

# Nonlinear port-Hamiltonian system identification from input-state-output data

Karim Cherifi<sup>1</sup>   Achraf El Messaoudi<sup>2</sup>   Hannes Gernandt<sup>1</sup>  
 Marco Roschkowski<sup>1</sup>

February 18, 2025

## Abstract

A framework for identifying nonlinear port-Hamiltonian systems using input-state-output data is introduced. The framework utilizes neural networks' universal approximation capacity to effectively represent complex dynamics in a structured way. We show that using the structure helps to make long-term predictions compared to baselines that do not incorporate physics. We also explore different architectures based on MLPs, KANs, and using prior information. The technique is validated through examples featuring nonlinearities in either the skew-symmetric terms, the dissipative terms, or the Hamiltonian.

**MSC:** 93B30, 93B15, 93C10, 68T07, 93B99

## 1 Introduction

Physics-based models used for simulating and controlling dynamical processes are dependable due to the well-validated and universally applicable physical laws, and they provide a high degree of interpretability. However, building such models from fundamental principles can be challenging, and their computational execution can be slow. In contrast, data-driven models, once trained, are typically easier to construct and can be executed more quickly. These approaches have gained traction for modeling intricate dynamical systems that are challenging or infeasible to describe explicitly, though they often face issues with generalizability and reliability beyond their training scope.

Given these complementary strengths and weaknesses, a hybrid approach that combines physics and Machine Learning (ML) is increasingly being adopted. This hybrid approach allows us to take advantage of the accuracy and generalizability of physics-based models while exploiting the flexibility and speed of

---

<sup>1</sup>Institute for Mathematical Modeling, Analysis and Computational Mathematics, University of Wuppertal, Gaußstraße 20, 42119 Wuppertal, Germany. {cherifi,gernandt,roschkowski}@uni-wuppertal.de.

<sup>2</sup>Sorbonne University, 4 place Jussieu, 75005 Paris, France. {achraf.el\_messaoudi}@etu.sorbonne-universite.fr.

ML methods. This integration has been particularly successful in several areas, such as the enhancement of physical models with deep networks to forecast complex dynamics [57], the development of neural ordinary differential equations (Neural-ODEs) [6], or the use of Physics-Informed Neural Networks (PINNs) [43] to solve forward and inverse problems for (partial) differential equations. When the solver is known, ML can be used to learn the residual or inductive biases, as seen in the Neural-ODE approach [6], which combines physics from learning and solver-based methods. In cases where everything must be learned end-to-end, approaches such as PhyDNet and MeshGraphNet have been developed to disentangle physical dynamics from unknown factors, enabling the learning of complex simulations [21, 41].

Hamiltonian neural networks represent a novel method for integrating extra physical knowledge into the dynamics that are to be identified. These networks leverage the Hamiltonian framework of dynamics to shape the neural architecture [20, 51, 16, 47]. Although these models perform better than non-physics based models, these Hamiltonian-based models inherently represent closed systems and they do not incorporate dissipation in the model.

In this study, we examine an expansion of Hamiltonian modeling, known as port-Hamiltonian (pH) systems, characterized as systems of ordinary differential equations structured as follows

$$\begin{aligned} \dot{x}(t) &= (J(x(t)) - R(x(t))) \nabla H(x(t)) + B(x(t))u(t), & x(0) &= x_0 \\ y(t) &= B(x(t))^\top \nabla H(x(t)), & t &\geq 0, \end{aligned} \quad (1)$$

where  $x \in \mathcal{X} \subseteq \mathbb{R}^n$  is the state vector,  $u \in \mathcal{U} \subseteq \mathbb{R}^m$  is the input vector, and  $y \in \mathcal{Y} \subseteq \mathbb{R}^m$  is the output vector. The Hamiltonian  $H : \mathcal{X} \rightarrow \mathbb{R}$  is a continuously differentiable function that is assumed to be bounded from below. The matrices  $J(x), R(x) \in \mathbb{R}^{n \times n}$ ,  $B(x) \in \mathbb{R}^{n \times m}$ , satisfy the following properties:

$$J(x) = -J^\top(x), \quad R(x) = R(x)^\top \geq 0. \quad (2)$$

Within this framework, the matrix function  $J$  signifies the internal energy-conserving connections within the system, accounting for reversible interactions. Furthermore, the framework incorporates dissipation in the model when  $R \neq 0$ , attributable to factors such as resistance, friction losses, load losses, and analogous effects.

The class of pH systems is becoming increasingly popular because it offers robust models that are inherently passive and can guarantee the stability of equilibria, see [36, 52] for an overview. Since the interconnection is through power or energy as universal quantities across several physical domains, the representation of the pH system offers a cohesive framework for numerical simulations of multi-physical systems [31] and has been applied to model various types of systems, including electrical power systems [17, 18], mechanical systems [42], fluid dynamics [5] and interacting particle systems [26].

The aim of this paper is to develop a method for identification of nonlinear pH systems based on ML, see also [7] for a recent overview of ML techniques for

pH systems. Various identification methods have been proposed for linear pH systems, i.e. when  $J$  and  $R$  are constant coefficient matrices and  $H$  is a quadratic function. For example, there is a pH version of the well-known Dynamic Mode Decomposition (pHDMD) [37], and approaches utilizing linear matrix inequalities (LMIs) [10, 45], optimization in the time-domain [48, 22, 23], subspace identification [35], frequency domain methods using the Loewner framework [3, 9, 8].

The extension to pH structure-preserving identification for nonlinear dynamics remains less explored. Recent advances were made in the context of circuits [38], or mechanical systems [12], or using Gaussian Processes [2, 58] or by using Autoencoders [44] and Pseudo-Hamiltonian systems [14]. These works have primarily focused on linear pH systems or have only partially addressed nonlinear systems by approximating specific components like the Hamiltonian or dissipation matrices or by using prior assumptions on the structure of the system matrices.

The invariance of pH systems under structure-preserving interconnection was recently used in [39] to speed up the training process by decomposing a given pH system into pH subsystems which are trained independently and the trained systems are then reassembled. This method was recently extended in [53] which approximates an internal port-Hamiltonian system based on input-output data for several time steps.

In this paper, we address this gap by focusing on the identification and learning of nonlinear port-Hamiltonian systems from input-state-output data. Our approach employs multilayer perceptrons (MLPs) designed to maintain the pH structure of the system to approximate each constituent component of the system, namely, the interconnection matrix  $J$ , the dissipation matrix  $R$ , the Hamiltonian  $H$ , and the input matrix  $B$ . By assigning dedicated MLPs to each matrix and incorporating a parametrization scheme, we ensure that the learned models strictly adhere to the pH structure. This method maintains the system’s physical integrity while utilizing neural networks’ universal approximation abilities to accurately model intricate nonlinear dynamics. In addition to the first architecture, we also experiment with the newly proposed Kolmogorov-Arnold Networks (KANs) and compare them with MLPs. Compared to the recent approach to identify nonlinear pH systems [53], we use input-state-output data and implement different versions of MLPs and KANs with and without prior knowledge and validate the method for various examples and settings.

The paper is structured as follows. In Section 2 we present our structure-preserving learning-based approaches using MLPs and KANs. In Section 3 we describe the training setup including the loss function. Finally, in Section 4 the identification approach is applied to various examples that showcase the strengths of the proposed framework.

## 2 Learning-based identification of port-Hamiltonian systems

In this section, we present different approaches that combine the general pH framework with neural networks and allow us to identify the nonlinear pH system structure from input-state-output data. More precisely, our aim is to approximate the Hamiltonian  $H$  and the system matrices  $J$ ,  $R$ , and  $B$  of the pH system (1) by using state-input-output data. To this end, we sample trajectories of the pH system (1) for various initial values  $x_0 \in \mathbb{R}^n$  and continuous input signals  $u : [0, \infty) \rightarrow \mathbb{R}^m$ . To generate a sufficiently rich amount of training data, we sample over different initial conditions  $x_0$  and different input trajectories  $u$ , see Section 3 for further details.

### 2.1 Parametrization of port-Hamiltonian systems

To preserve the port-Hamiltonian structure of the state-dependent system matrices  $J(x)$  and  $R(x)$  during the identification process, we build on a structured representation for the linear case from [45, 46, 48] using the following reshaping operation that maps vectors to full matrices

$$\text{vtf}_{n,m} : \mathbb{R}^{n \cdot m} \rightarrow \mathbb{R}^{n \times m}, \quad v = (v_i)_{i=1}^{nm} \mapsto \begin{bmatrix} v_1 & v_{n+1} & \cdots & v_{m(n-1)+1} \\ v_2 & v_{n+2} & \cdots & v_{m(n-1)+2} \\ \vdots & \vdots & & \vdots \\ v_n & v_{2n} & \cdots & v_{nm} \end{bmatrix}.$$

This reshaping operation is used in conjunction with the state-dependent parameter functions

$$\theta_J : \mathcal{X} \rightarrow \mathbb{R}^{n^2}, \quad \theta_R : \mathcal{X} \rightarrow \mathbb{R}^{n^2}, \quad \theta_B : \mathcal{X} \rightarrow \mathbb{R}^{mn}, \quad \theta_H : \mathcal{X} \rightarrow \mathbb{R}, \quad (3)$$

to represent the matrix-valued functions  $J$ ,  $R$ ,  $B$  and the Hamiltonian  $H$  in the pH system representation (1) as

$$\begin{aligned} J(x) &= \text{vtf}_{n,n}(\theta_J(x))^\top - \text{vtf}_{n,n}(\theta_J(x)), \\ R(x) &= \frac{1}{\sqrt{n}} \text{vtf}_{n,n}(\theta_R(x)) \text{vtf}_{n,n}(\theta_R(x))^\top, \\ B(x) &= \text{vtf}_{n,m}(\theta_B(x)), \\ H(x) &= \theta_H(x), \end{aligned} \quad (4)$$

which, by construction, leads to  $J(x) = -J(x)^\top$  and  $R(x) = R(x)^\top \geq 0$ .

To improve computational efficiency in the identification of linear pH systems [45, 46], upper triangular parametrizations are used instead of the full parametrization  $\text{vtf}$  in (4). The same strategy could be used to maintain the pH structure for the nonlinear scenario, resulting in a point-wise Cholesky factorization of  $R$ . However, we do not consider reshaping operations that map to upper triangular matrices as in [45, 46] here for several reasons. First, we

consider approximations of the parameter function  $\theta_R$  by deep neural networks where most of the parameters are located in hidden layers, which implies that the parameter reduction using more advanced reshaping operations results in a limited reduction of parameters. Second, for large matrices, the number of summands that appear in the resulting product matrix increases for the bottom rows and rightmost columns, which might introduce additional scaling problems. For this reason, we introduce the additional factor in parametrization  $\frac{1}{\sqrt{n}}$  following standard practice in the machine learning community, for example, used in the product of keys and queries in attention layers [54].

The computational effort and the accuracy of the identification can be further improved by using prior information on the system. In nonlinear system identification it is common to incorporate ansatz functions in the pH system identification. If only limited prior knowledge is available, there are methods such as SINDy [4] where large sets of ansatz functions are prescribed that require sparse identification methods that select only a few of these ansatz functions appearing in the system equations. In contrast to this, we have a very particular pH system structure (1) that cannot be directly incorporated into the SINDy framework.

To incorporate prior information in the pH identification we may assume that for some of the pH matrix coefficients  $R$ ,  $J$ ,  $B$  and  $H$  there are certain ansatz functions

$$a_{\bullet}(x) := \begin{bmatrix} a_{\bullet,1}(x) \\ \vdots \\ a_{\bullet,N_{\bullet}}(x) \end{bmatrix}, \quad a_{\bullet,i} : \mathbb{R}^n \rightarrow \mathbb{R}, \quad i = 1, \dots, N_{\bullet}, \quad \bullet \in \{R, J, B, H\}.$$

Then, as an alternative to (4) we obtain the following parametrization

$$\begin{aligned} J(x) &= \text{vtf}_{n,n}(\theta_J^{\text{pri}} a_J(x))^\top - \text{vtf}_{n,n}(\theta_J^{\text{pri}} a_J(x)), \\ R(x) &= \frac{1}{\sqrt{n}} \text{vtf}_{n,n}(\theta_R^{\text{pri}} a_R(x))^\top \text{vtf}_{n,n}(\theta_R^{\text{pri}} a_R(x)), \\ H(x) &= \theta_H^{\text{pri}} a_H(x), \quad B(x) = \text{vtf}_{n,m}(\theta_B^{\text{pri}} a_B(x)), \end{aligned} \quad (5)$$

using constant parameter matrices  $\theta_J^{\text{pri}} \in \mathbb{R}^{n^2 \times N_J}$ ,  $\theta_R^{\text{pri}} \in \mathbb{R}^{n^2 \times N_R}$ ,  $\theta_H^{\text{pri}} \in \mathbb{R}^{1 \times N_H}$  and  $\theta_B^{\text{pri}} \in \mathbb{R}^{nm \times N_B}$  which need to be adjusted to the given input-state-output data.

For the special case  $N = 1$  and  $a_1 = 1$ , we obtain constant  $R$ ,  $J$  and  $B$  matrices, which leads to

$$J = \text{vtf}_{n,n}(\theta_J^{\text{pri}})^\top - \text{vtf}_{n,n}(\theta_J^{\text{pri}}), \quad R = \frac{1}{\sqrt{n}} \text{vtf}_{n,n}(\theta_R^{\text{pri}})^\top \text{vtf}_{n,n}(\theta_R^{\text{pri}}). \quad (6)$$

Moreover, for various pH systems it is reasonable to assume that the Hamiltonian is nonnegative, quadratic and described as

$$H(x) = \frac{1}{2} x^\top Q x, \quad Q = \frac{1}{\sqrt{n}} \text{vtf}_{n,n}(\theta_Q^{\text{pri}})^\top \text{vtf}_{n,n}(\theta_Q^{\text{pri}}), \quad (7)$$

for some parameter  $\theta_Q^{\text{pri}} \in \mathbb{R}^{n^2}$ . This inherently guarantees non-negativity, thus eliminating the need to constrain  $\theta_H^{\text{pri}}$  to be positive semi-definite during optimization [45]. If (6) and (7) are assumed, then we obtain the parametrization for linear pH systems from [45], but using a full parametrization instead of upper triangular matrices. As some features might have small magnitudes, we also consider the setting where  $\nabla_x H(x) = Qx + b$  for some  $b \in \mathbb{R}^n$ . This allows us to standard-scale the states (subtracting their mean and dividing by their standard deviation) before processing with the neural network to avoid numerical underflows and gradient issues. Moreover, this allows us to identify so-called shifted Hamiltonians where the constant input signals in the system might lead to a nonzero equilibrium points, see e.g. [18], which cannot be modeled by the quadratic Hamiltonian of the form (7).

In our pH identification method, we can flexibly combine parametrizations with and without prior knowledge (5) and (4), respectively, for each of the different coefficient matrices  $J, R, B$  and the Hamiltonian  $H$ , e.g. one is allowed to parametrize  $J$  and  $B$  via (4),  $R$  via some ansatz functions (5) and the Hamiltonian  $H$  as a quadratic function (7).

## 2.2 Neural network architectures

The approximation of the parameter functions (3) is based on Multi-Layer Perceptrons (MLPs) and Kolmogorov-Arnold Networks (KANs) as illustrated in Figure 1. Each state variable  $x_i$  corresponds to a neuron  $i_i$  in the input layer, each components of the parameter function  $\theta_{\bullet,i}$  where  $\bullet \in \{J, B, R, H\}$  correspond to a neuron  $\mathbf{o}_i$  in the output layer and there are neurons  $\mathbf{h}_i^{(j)}$  in the hidden layers. Furthermore, the size of the output layers are given by  $n_B = nm$ ,  $n_H = 1$ , and  $n_J = n_R = n^2$ .

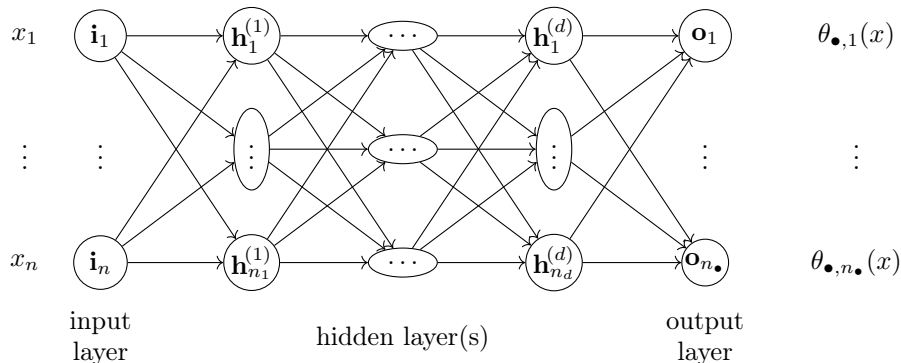


Figure 1: Generic MLP or KAN architecture used for approximation of the parameter functions  $\theta_{\bullet}$  where  $\bullet \in \{J, B, R, H\}$ .

MLPs are the most basic type of deep neural network. They are fully connected feedforward artificial neural networks [24], but despite their simplicity,

they inherit a universal approximation property that makes them capable of approximating any continuous function in a compact domain uniformly with any prescribed accuracy, provided that a sufficient amount of data is available, see [11, 25].

MLPs can be mathematically defined as follows

$$\varphi_l = \sigma_l(W_l\varphi_{l-1} + b_l), \quad l = 1, \dots, L, \quad (8)$$

where  $l$  is the index of the current layer,  $\varphi_{l-1} \in \mathbb{R}^{n_l}$ ,  $n_l$  represents the number of neurons in the  $l$ th layer,  $W_l \in \mathbb{R}^{n_l \times n_{l-1}}$  models the weight matrix of the last layer,  $b_l \in \mathbb{R}^{n_l}$  is the bias vector of the last layer, and  $\sigma_l : \mathbb{R}^{n_{l-1}} \rightarrow \mathbb{R}^{n_l}$  is a typically nonlinear activation function to incorporate the system's inherent nonlinearities (if present). Moreover, the layers  $l = 0$  and  $l = L$  are called *input* and *output layer*, respectively.

When fully assembled, the MLP transforms an input feature vector  $\varphi_0 \in \mathbb{R}^{n_0}$  into an output vector  $\varphi_L \in \mathbb{R}^{n_L}$ .

$$\text{MLP}_\phi : \mathbb{R}^{n_0} \rightarrow \mathbb{R}^{n_L}, \quad \varphi_0 \mapsto \varphi_L = \sigma_L(W_L\varphi_{L-1} + b_L),$$

where  $\phi = \{(W_1, b_1), \dots, (W_L, b_L)\}$  represents the set of trainable parameters.

In our proposed pH identification, we train the parameters of several MLPs to approximate the parameter functions

$$\theta_\bullet(x) \approx \text{MLP}_{\bullet, \phi}(x), \quad \bullet \in \{J, R, B, H\}.$$

Each neural network is then used to recover the system matrices or evaluate the nonlinear pH model directly.

In addition to MLPs, we also explore the use of multilayer KANs. They have recently been proposed based on the Kolmogorov-Arnold representation theorem [30]. This theorem established that a multivariate continuous function on a bounded domain, can be written as a finite composition of continuous functions of a single variable and the addition operation. More specifically, any continuous  $f : [0, 1]^n \rightarrow \mathbb{R}$  can be represented by

$$f(x) = f(x_1, \dots, x_n) = \sum_{q=1}^{2n+1} \Phi_q \left( \sum_{p=1}^n \phi_{q,p}(x_p) \right), \quad (9)$$

where  $\phi_{q,p} : [0, 1] \rightarrow \mathbb{R}$  and  $\Phi_q : \mathbb{R} \rightarrow \mathbb{R}$  are some univariate continuous functions.

In terms of architecture, KANs are similar to MLPs. The difference is that, for each neuron, a function is learned instead of a single weight. In order to learn the nonlinear activation functions in KANs, they are represented by a weighted combination of a basis activation function  $b$  and a  $B$ -spline,

$$\Psi(x) = w_b b(x) + w_s \text{spline}(x), \quad \text{spline}(x) = \sum_i c_i B_i(x), \quad (10)$$

where  $B_i$  is a polynomial of degree  $k$ , and  $b$  is a basis activation function, and the weights  $c_i$ ,  $w_b$ , and  $w_s$  are trainable parameters. Learning functions instead

of individual weights in MLPs introduces significant computational challenges. Nonetheless, [30] demonstrates that for some applications only a small number of neurons in KANs are required to match the precision of a large MLP network. Fewer neurons also improve network interpretability, making KANs advantageous for efficient function approximation in low-dimensional spaces and capturing compositional structures in high-dimensional data.

### 3 Training setup

In this section, we discuss the data used to train the neural networks, the baseline, and the loss function. We also discuss the error measures used to compare the different models. All experiments were conducted in PyTorch [40]. Following the concept from [53], we utilize PyTorch’s autograd function to compute the gradient of  $\theta_H$  at input  $x \in \mathbb{R}^n$ , which approximates  $\nabla_x H(x)$ .

#### 3.1 Input-state-output data generation

The generation of data is similar to [39]. We uniformly sample initial states  $x_{i,0} \sim U(x_{i,\min}, x_{i,\max})$ ,  $i = 1, \dots, n$ , where the choice of  $x_{i,\min}$  and  $x_{i,\max}$  depends on the particular application. The trajectories are generated by using SciPy’s `odeint` function [55]. Training and evaluation trajectories consist of 10 second-long trajectories with  $\Delta t = 0.01$  resulting in trajectories of 1000 data points each. We use 1000 evaluation trajectories for each problem that are different from the training trajectories which is enough to obtain a robust and reproducible error estimate. We consider the use of 10, 30, 100, 300 and 1000 training trajectories to obtain the results of our method in different data size regimes. Moreover, we evaluate long-term behavior by inspecting another 20 trajectories over a 100 second period which do not belong to the training data set.

We follow [53] to sample the input signal

$$u(t) = \sum_{k=1}^N a \sin(2\pi k f_0 t + \phi_k), \tag{11}$$

with  $f_0 = 0.1$ ,  $N = 40$ , and random phases  $\phi_k$  that are uniformly sampled from  $[0, 2\pi)$ . The prediction targets are the time derivatives of the states  $\dot{x}$  and the outputs  $y$ . Using the equations of the pH system (1), this also allows us to determine the values of the derivatives  $\dot{x}$ . However, in practical situations, it is common to estimate  $\dot{x}$  from observed trajectories. A significant portion of the SINDy project [4] has been devoted to this. For simplicity, we used instead the values given by the system equation with true coefficients.

#### 3.2 Loss function and optimization

The dataset for training consists of trajectories  $\{x_k(t_j) = x(t_j; x_{0,k}, u_k) \mid j = 1, \dots, N_t\}$ , generated from different starting conditions  $x_{0,k}$  and input signals

$u_k$ ,  $k = 1, \dots, N_{\text{tra}}$ , as outlined in Section 3.1. All trajectories in the data set are concatenated

$$(x_1(t_1), \dots, x_1(t_{N_t}), \dots, x_{N_{\text{tra}}}(t_1), \dots, x_{N_{\text{tra}}}(t_{N_t})) \in \mathbb{R}^{N_t N_{\text{tra}} n} \quad (12)$$

and from this concatenated trajectories. In order to lessen the computational demands of weight optimization, instead of utilizing the entire data set (12), we employ a common deep learning strategy that creates a minibatch  $\mathcal{B}$ . This is done by randomly selecting  $|\mathcal{B}| > 0$  entries of (12)

$$l \mapsto (j(l), k(l)), \quad l = 1, \dots, |\mathcal{B}|.$$

Moreover, using the system equations (1), the data set uniquely specifies the values of the state-derivatives  $\dot{x}_k(t_j) = \dot{x}(t_j; x_{0,k}, u_k)$  and the outputs  $y_k(t_j) = y(t_j; x_{0,k}, u_k)$ . We standard-scale states and inputs before processing them with our neural networks. More specifically, given  $1 \leq i \leq n$ ,  $1 \leq q \leq m$  we compute

$$\begin{aligned} \tilde{\mu}_{x_i} &= \frac{1}{N_t \cdot N_{\text{tra}}} \sum_{k=1}^{N_{\text{tra}}} \sum_{j=1}^{N_t} x_{k,i}(t_j) \\ \tilde{\sigma}_{x_i} &= \sqrt{\frac{1}{N_t \cdot N_{\text{tra}} - 1} \sum_{k=1}^{N_{\text{tra}}} \sum_{j=1}^{N_t} (x_{k,i}(t_j) - \tilde{\mu}_{x_i})^2} \\ \tilde{\mu}_{u_q} &= \frac{1}{N_t \cdot N_{\text{tra}}} \sum_{k=1}^{N_{\text{tra}}} \sum_{j=1}^{N_t} u_{k,q}(t_j) \\ \tilde{\sigma}_{u_q} &= \sqrt{\frac{1}{N_t \cdot N_{\text{tra}} - 1} \sum_{k=1}^{N_{\text{tra}}} \sum_{j=1}^{N_t} (u_{k,q}(t_j) - \tilde{\mu}_{u_q})^2} \end{aligned}$$

and use as the inputs to the neural network

$$\begin{aligned} (\tilde{x}_1, \dots, \tilde{x}_n) &= \left( \frac{x_1 - \tilde{\mu}_{x_1}}{\tilde{\sigma}_{x_1}}, \dots, \frac{x_n - \tilde{\mu}_{x_n}}{\tilde{\sigma}_{x_n}} \right), \\ (\tilde{u}_1, \dots, \tilde{u}_m) &= \left( \frac{u_1 - \tilde{\mu}_{u_1}}{\tilde{\sigma}_{u_1}}, \dots, \frac{u_m - \tilde{\mu}_{u_m}}{\tilde{\sigma}_{u_m}} \right). \end{aligned}$$

The minibatch is then given by

$$(\tilde{x}_{k(l)}(t_{j(l)}), \dot{x}_{k(l)}(t_{j(l)}), \tilde{u}_{k(l)}(t_{j(l)}), y_{k(l)}(t_{j(l)}))_{l=1}^{|\mathcal{B}|}.$$

The corresponding predictions for  $\dot{x}$  and  $y$  of our model are indicated by  $\hat{x}$  and  $\hat{y}$ , respectively.

Our objective is to minimize the error that is normalized over the training

minibatch for each target, i.e.

$$\begin{aligned} \mathcal{L}(\hat{x}, \dot{x}, \hat{y}, y) = & \frac{1}{|\mathcal{B}|} \sum_{l=1}^{|\mathcal{B}|} \sum_{i=1}^n \frac{|\dot{x}_{k(l),i}(t_{j(l)}) - \widehat{\dot{x}}_{k(l),i}(t_{j(l)})|^2}{\sigma_{\dot{x}_i}^2} \\ & + \gamma \sum_{i=1}^m \frac{|y_{k(l),i}(t_{j(l)}) - \widehat{y}_{k(l),i}(t_{j(l)})|^2}{\sigma_{y_i}^2} \end{aligned} \quad (13)$$

where  $\gamma > 0$  weights the output loss and we typically use  $\gamma = 0.25$  because correctly predicting the states is more crucial for long-term forecasting. In our experiments, we noticed that the validation error do not strongly depend on the exact value of  $\gamma$ . All the choices of  $\gamma$  considered resulted in the same order of magnitude in the error measures considered.

Moreover,  $\sigma_{\dot{x}_i}$  and  $\sigma_{y_j}$  represent the standard deviation of  $\dot{x}_i$  and  $y_i$  over the current training minibatch, respectively, i.e.

$$\sigma_{\dot{x}_i} = \sqrt{\frac{1}{|\mathcal{B}| - 1} \sum_{l=1}^{|\mathcal{B}|} \left( \dot{x}_{k(l),i}(t_{j(l)}) - \frac{1}{|\mathcal{B}|} \sum_{l=1}^{|\mathcal{B}|} \dot{x}_{k(l),i}(t_{j(l)}) \right)^2}$$

where  $(\dot{x}_{k(l),i}(t_{j(l)}))_{l=1}^{|\mathcal{B}|}$  is the current training minibatch for the feature  $\dot{x}_i$ . Commonly, different states have different orders of magnitude and, consequently, all states have to be rescaled to have the same order of magnitude, e.g., as in [44]. For the considered examples, we found that our setup works well without rescaling any relevant quantities by simply modifying the loss function to account for the standard deviation of each target as described above.

Our main evaluation objective is the following *normalized mean absolute error*

$$\text{NMAE}(\dot{x}_i, \widehat{\dot{x}}_i) = \sum_{i=1}^n \frac{|\dot{x}_i - \widehat{\dot{x}}_i|}{\sigma_{\dot{x}_i}},$$

where the standard deviation is calculated for all points in the evaluation data set. We use here a normalized MAE, because we do not rescale the state derivatives  $\dot{x}$ , which implies that derivatives of different states can have vastly different magnitudes.

We point out that the error on the derivatives of the states is more important for long-term forecasting compared to the error on the output, as these accumulate during forecasting.

Incorporation of system output is not only being used as an auxiliary target to improve the prediction of  $\dot{x}$ , but also because of the system-theoretic properties related to system interconnection, which require access to correct system outputs.

For MLPs, we use  $d = 3$  hidden layers with each having 64 neurons and with the swish activation function  $\text{swish} : \mathbb{R} \rightarrow \mathbb{R}$ , see [15], that is given by

$$\text{swish}(x) := \frac{x}{1 + e^{-x}}. \quad (14)$$

Moreover, we use layer normalization [28] at hidden layers. For KAN, we use a grid size of 5, spline order 3 and the base activation function  $b = \text{swish}$  in (10). We use a hidden dimension of 3 with 3 hidden layers, since KANs are typically more expensive and expressive than MLPs. The efficient open-source code from [1] is used to implement KANs in PyTorch.

To optimize the parameters, we use the Adam optimizer [27] with decoupled weight decay [33] and using minibatches. The default minibatch size is set to 256. As there is a large variety of training setups, some with very few and some with a larger number of trajectories, we typically scale the number of training epochs inversely proportional to the number of training trajectories. We employ cosine annealing [34] with warmup [19] to schedule the learning rate. By default we use for AdamW the learning rate 0.001,  $(\beta_1, \beta_2) = (0.9, 0.999)$  and weight decay 0.01.

### 3.3 Baseline

We compare the identified pH systems with a non-physics-informed baseline. This baseline can be seen as a black-box system model defined as

$$\begin{bmatrix} \dot{x}_{\text{pred}} \\ y \end{bmatrix} = f_{\text{base}}(x, u).$$

The function  $f_{\text{base}}$  is parametrized using an MLP with the same depth as those used in the pH structure-preserving method. To ensure a fair comparison, we scaled the width of the MLPs so that the total parameter count equals that of our default strategy.

## 4 Numerical experiments

In this section, we demonstrate our identification approach for various types of port-Hamiltonian systems, each showcasing different aspects of system nonlinearity. Specifically, we examine examples that are nonlinear either in the skew-symmetric matrix  $J$  or the dissipation matrix  $R$ , and may feature quadratic or non-quadratic Hamiltonians. A computer equipped with an AMD Ryzen 9 5900X 12-Core processor and 32 GB of RAM was used to conduct the experiments. The code used to replicate all numerical experiments presented in the paper is available at <https://github.com/trawler0/Port-Hamilton-System-Identification-with-PINNS>.

### 4.1 Mass spring system

We consider a mass spring system from [39] which is composed of a mass  $m_1$  that is attached to a wall and a second mass  $m_2$  by two springs with corresponding spring constants  $k_1, k_2 > 0$ . The relative elongation  $q_i$  and the impulse  $p_i$  of the masses lead to the states  $(x_1, x_2) = (q_1, p_1)$  and  $(x_3, x_4) = (q_2, p_2)$ , respectively. Furthermore, as proposed in [32], we introduce a nonlinear damping force  $F_i =$

$b_i m_i^{-3} \dot{p}_i^3$ ,  $i = 1, 2$ , for some  $b_i \geq 0$  acting on each of the subsystems. The Hamiltonian for each subsystem  $H_i(x_i)$  is given by

$$H_i(x_i) = \frac{p_i^2}{2m_i} + \frac{k_i q_i^2}{2},$$

which leads to the Hamiltonian  $H = H_1 + H_2$  for the interconnected system which is given by

$$\dot{x} = (J - R(x))\nabla H(x) + Bu(t),$$

where the skew-symmetric matrix  $J$ , the damping matrix  $R$ , and the input matrix  $B$  are given by

$$J = \begin{bmatrix} 0 & 1 & 0 & 0 \\ -1 & 0 & 1 & 0 \\ 0 & -1 & 0 & 1 \\ 0 & 0 & -1 & 0 \end{bmatrix}, \quad R(x) = \begin{bmatrix} 0 & 0 & 0 & 0 \\ 0 & \frac{b_1 p_1^2}{m_1^2} & 0 & 0 \\ 0 & 0 & 0 & 0 \\ 0 & 0 & 0 & \frac{b_2 p_2^2}{m_2^2} \end{bmatrix}, \quad B = \begin{bmatrix} 0 & 0 \\ 1 & 0 \\ 0 & 0 \\ 0 & 1 \end{bmatrix}$$

and  $u$  represents forces that are acting on each of the masses. The amplitude of the input is set to  $a = 0.4$  in order to rescale the combined sinusoidal signals and sample the initial states uniformly from  $(q_{1,0}, p_{1,0}, q_{2,0}, p_{2,0}) \sim [-0.5, 0.5]^4$ .

To obtain the simulation data for the learning-based system identification task, we choose the model parameters that are listed in Table 1. In the above

symbol	meaning	value	unit
$m_1$	mass 1	1	[kg]
$m_2$	mass 2	1.5	[kg]
$b_1, b_2$	damping coefficient	2	-
$k_1$	spring constant 1	1	[N/m]
$k_2$	spring constant 2	0.1	[N/m]

Table 1: System parameters for the interconnected mass spring system

example, we considered a quadratic Hamiltonian. It is possible to modify the example to obtain non-quadratic Hamiltonians, by applying hardening constraints to the spring, as discussed in [32], or by considering a Duffing-type oscillator, as shown in [13].

As a first experiment, we constructed a pH system based on our default MLP architecture. Multiple experiments were carried out for different numbers of training trajectories ranging from 10 to 1000. The normalized MAE is shown in Figure 2. The error is averaged over different test trajectories with random initial conditions that were not part of the training set. The validation error decreases as the number of trajectories used for training increases. The pH implementation is compared with a baseline without any prior physical information. In low data regimes, both pH and the baseline exhibit similar performance.

However, when enough data is available for training the pH model clearly outperforms the baseline. In addition, we also train a pH prior that incorporates prior information about the model by assuming that the matrix  $J$  in the pH model is constant and the Hamiltonian to be quadratic. The resulting pH prior model achieves a lower error than both the general pH model and the baseline. This confirms that incorporating physical knowledge and prior information on the model helps reduce the error and requires a lower amount of training data. For example, for the same prescribed error  $\text{NMAE} = 3 \cdot 10^{-4}$ , pH prior model needs only 30 trajectories, while the baseline requires more than 1000 trajectories. In a real setup, where the data might be limited, this difference can be crucial to get a reasonably good model.

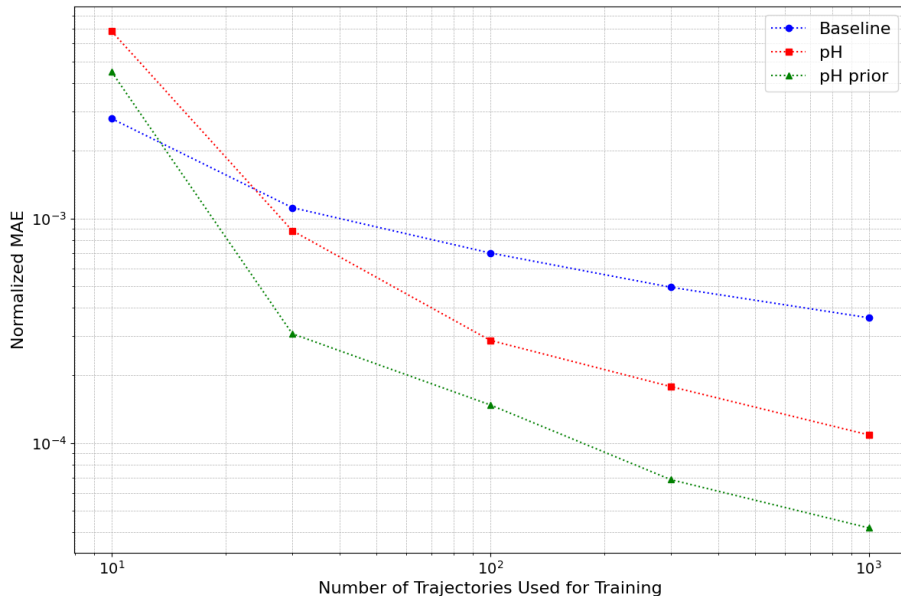


Figure 2: Average validation error for the spring model as a function of varying quantities of trajectories employed in training a baseline model, a default pH setup, and a pH setup incorporating prior knowledge.

In order to investigate if the chosen architecture is the right one and to confirm that our model actually learned the physics and not the system’s behavior in the time interval spanned by the training data, we consider the long-term behavior of a single state trajectory. The system is trained using 10 training trajectories for the time interval until 10 seconds then tested until 100 seconds. Here, we use the classical Runge-Kutta scheme for the forecasting to have a high order of accuracy.

The resulting trajectory for the momentum of the default pH model is shown in Figure 3 and compared to the true trajectory. It is clear from the figure that the pH system is able to predict the trajectory of the state well beyond the data

used for training. In addition, the same figure shows two other configurations. The first is a shallow network with only one hidden layer. The other is our default pH configuration with a shorter training time of 10 times fewer epochs. Although both of these configurations can replicate the data used for training, they start to deviate for longer prediction times. It becomes evident that both the training time and the network depth are crucial hyperparameters for our method.

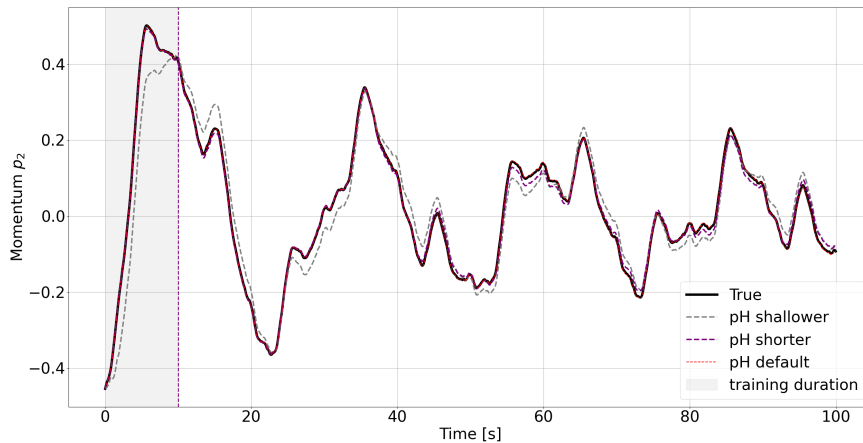
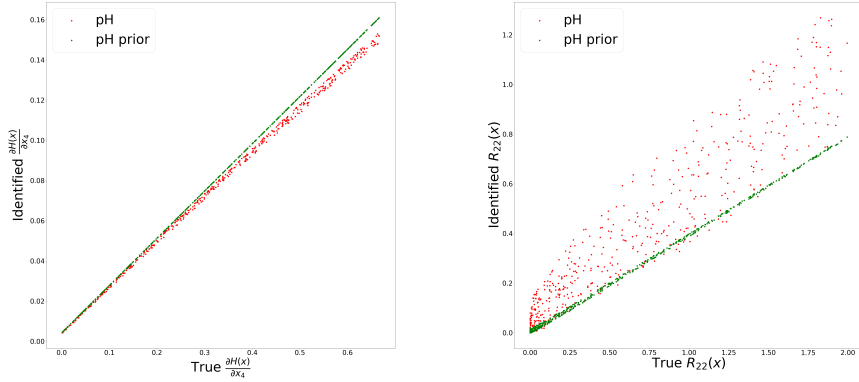


Figure 3: The trajectory of the momentum  $p_2$  of the spring for different pH training setups. The vertical line at 10s indicates the final time using in the training of the trajectories.

An interesting question is how well our method performs in identifying the true system parameters. One cannot expect to fully recover the system's coefficients since one could, for example, add a constant to the Hamiltonian or move a scaling factor from the  $J(x) - R(x)$  term to the Hamiltonian. However, in practice, we observed strong correlations between the identified parameters and the true parameters, typically even more if one uses prior knowledge. Figure 4 shows scatter plots that demonstrate this behavior. We plot the true value of an observable (gradient of the Hamiltonian or dissipation) against the identified value given different state values. We only consider the entries that are nonlinear. A cumulation of the resulting points on a straight line would mean that the two observables are correlated. In addition, if the line represents the identity function with a slope of 1, every identified value is equal to the true value, thus, closer slope values to 1 result in better identification of the true system parameters. For example, for the dissipation plot in 4b, we can observe that the values for pH prior are more grouped together in line while the values for pH are more scattered. This means that the pH prior is more effective in preserving the original entries for the dissipation matrix. For the Hamiltonian

in 4a, we notice that the identified and true values are correlated for pH. It is even better for the model with incorporated prior knowledge where the slope is close to 1 meaning that we perfectly recover the entries of the true Hamiltonian.



(a) The derivative of  $H$  with respect to  $x_4$  (b) Diagonal entry  $R_{22}$  of the matrix  $R$

Figure 4: Comparison between identified system parameters and true system parameters for changing state values  $x$ .

We conclude this example with a comparison between different prior heuristics in Figure 5. The performance of the default pH implementation called pH in Figure 5 can be improved by including the prior knowledge that  $J$  and  $B$  are constant and considering the general parametrization for  $R$  and the Hamiltonian  $H$ . This is called pH MLP prior in Figure 5. If in addition the entries in  $R$  are assumed to be quadratic functions, the performance of the system can be further improved, as shown in the pH quadratic prior. However, if the wrong prior is assumed (pH fully linear prior in Figure 5) for example by assuming that all matrices coefficients are constant including  $R$ , then the error does not improve even when increasing the number of trajectories. Assuming linearity in the model can result in significant inaccuracies. The presented nonlinear framework is essential for this example, as linear approaches commonly available in the literature are insufficient.

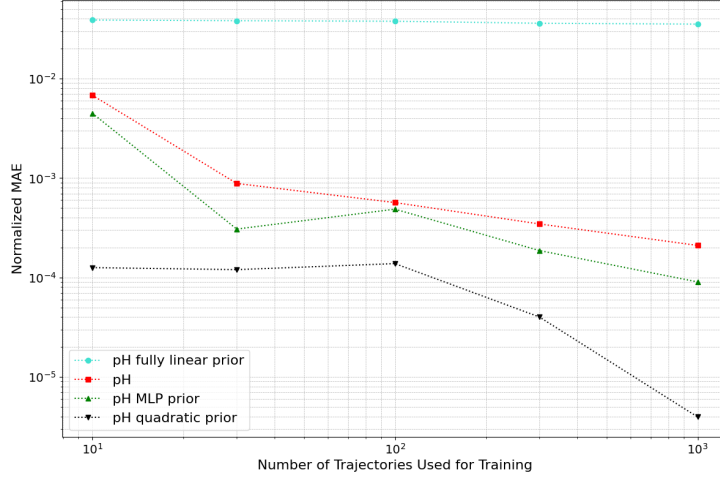


Figure 5: NMAE in function of number of trajectories used for training for different priors for the spring example.

## 4.2 Magnetically levitated ball

In this example from [2], we consider the model of an iron ball of mass  $m$  in the magnetic field of a controlled inductor. The states of this system are the vertical position of the ball  $x_1$ , its momentum  $x_2$  and the magnetic flux  $x_3$  and it can be written in the form

$$\dot{x} = \left( \underbrace{\begin{bmatrix} 0 & 1 & 0 \\ -1 & 0 & 0 \\ 0 & 0 & 0 \end{bmatrix}}_{=J} - \underbrace{\begin{bmatrix} 0 & 0 & 0 \\ 0 & c \cdot |x_2| & 0 \\ 0 & 0 & \frac{1}{R} \end{bmatrix}}_{=R(x)} \right) \nabla H(x) + \underbrace{\begin{bmatrix} 0 \\ 0 \\ 1 \end{bmatrix}}_{=:B} u(t)$$

with the non-quadratic Hamiltonian that is given by

$$H(x) = \frac{1}{2m}x_2^2 + \frac{1}{2} \frac{x_3^2}{L(x_1)}.$$

For simulations, we choose the inductance  $L(x_1) = (0.1 + x_1^2)^{-1}$  and use the model parameters listed in Table 2 and set  $m = 0.1$  for the mass of the ball.

symbol	meaning	value	unit
$m$	ball mass	0.1	[kg]
$L(x_1)$	inductivity at height $x_1$	$(0.1 + x_1^2)^{-1}$	[H]
$R$	electrical resistance	0.1	[Ω]
$c$	drag coefficient	1	-

Table 2: Iron Ball System Parameters

The amplitude of the input is set to  $a = 1$  to rescale the signal and sample the initial states uniformly from  $(x_{1,0}, x_{2,0}, x_{3,0}) \sim [-0.5, 2] \times [-0.2, 0.2] \times [-3, 5]$ . As in the previous example, we consider the comparison between a baseline without any physical knowledge, our default pH model and a pH model with prior knowledge about which parts of the model are nonlinear. The results for different numbers of trajectories in the training set are shown in Figure 6. We notice that the validation error decreases as the number of trajectories increases.

The plot in Figure 6 indicates that our default pH implementation outperforms the baseline and that the incorporation of prior knowledge can be helpful to increase prediction accuracy. Furthermore, adding prior physical knowledge helps train the model with less data.

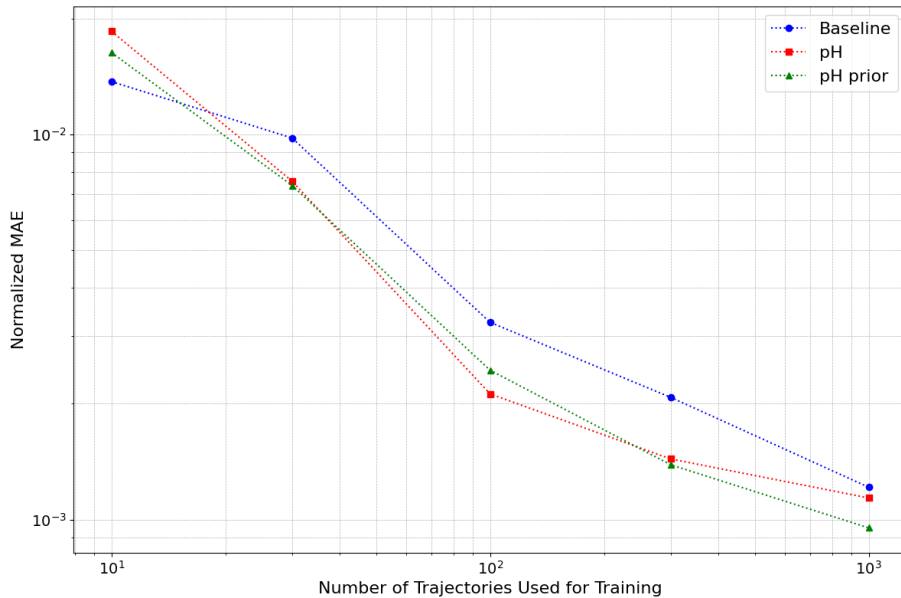


Figure 6: Average validation error for the ball example as a function of varying quantities of trajectories employed in training a baseline model, a default pH setup, and a pH setup incorporating prior knowledge.

To study the long-term behavior of the identified models, we consider state trajectories for the ground truth, the baseline model, the default pH model and a pH model where  $J$  and  $B$  are assumed to be constant. In Figure 7, as an example, we show the state trajectory of the momentum for a random initial value not in the training set. The models were trained with  $N_{\text{tra}} = 1000$  trajectories. During the first 10s on which the model was trained, all models behaved reasonably well. Although we could have assumed from Figure 6 that the baseline would behave similarly to the pH models, we can see from Figure 7 that the baseline deviates significantly when doing forecasting after the initial 10 seconds because it does not capture the physics of the system. This also

indicates that although the NMAE used for validation shows how good a model is for a given time interval, it may not be the best metric for the prediction error.

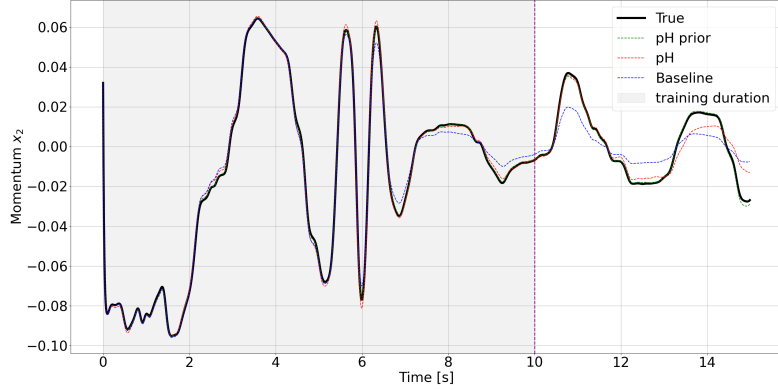


Figure 7: State trajectory of the ball example for the ground truth, baseline, pH and pH with prior knowledge. The model is trained using the first 10s of 1000 trajectories then tested for prediction up to 15s.

### 4.3 Permanent Magnetic Synchronous Motor (PMSM)

Consider the nonlinear dynamics of a 3-phase Permanent Magnet Synchronous Motor (PMSM) in the  $dq$ -coordinates which is described in [49, 56] using the pH formulation as follows:

$$\begin{bmatrix} \dot{\varphi}_d \\ \dot{\varphi}_q \\ \dot{p} \end{bmatrix} = \left( \underbrace{\begin{bmatrix} 0 & 0 & \varphi_q \\ 0 & 0 & -\varphi_d - \Phi \\ -\varphi_q & \varphi_d + \Phi & 0 \end{bmatrix}}_{=J(x)} - \underbrace{\begin{bmatrix} r & 0 & 0 \\ 0 & r & 0 \\ 0 & 0 & \beta \end{bmatrix}}_{=R} \right) \underbrace{\begin{bmatrix} \frac{\varphi_d}{L} \\ \frac{\varphi_q}{L} \\ \frac{p}{J_m} \end{bmatrix}}_{=\nabla H(x)} + \underbrace{\begin{bmatrix} 1 & 0 \\ 0 & 1 \\ 0 & 0 \end{bmatrix}}_{=B} \begin{bmatrix} v_d \\ v_q \end{bmatrix},$$

where the state vector  $x$  is composed of the stator magnetic fluxes  $\varphi_d$ ,  $\varphi_q$ , and the rotor momentum  $p$ . Moreover,  $\Phi$  is the permanent magnet flux of the rotor,  $L$  is the phase inductance,  $r$  is the stator resistance,  $J_m$  is the rotor moment of inertia, and  $\beta \geq 0$  is the viscous friction coefficient. Furthermore, the control inputs  $v_d$  and  $v_q$  are the stator voltages and the Hamiltonian is a quadratic function that is given by

$$H(x) = \frac{\varphi_d^2}{2L} + \frac{\varphi_q^2}{2L} + \frac{p^2}{2J_m}.$$

To obtain the simulation data for the learning-based system identification task, we choose the model parameters that are listed in Table 3.

symbol	meaning	value	unit
$J_m$	inertia	0.012	$[\text{kg} \cdot \text{m}^2]$
$L$	phase inductance	$3.8 \cdot 10^{-3}$	$[\text{H}]$
$\beta$	viscous friction coefficient	0.0026	$[\text{Nms/rad}]$
$r$	phase resistance	0.225	$[\Omega]$
$\Phi$	constant rotor magnetic flux	0.17	$[\text{Wb}]$

Table 3: PMSM System Parameters

For the amplitude of the input, we use  $a = 5$  to scale the signal and sample the initial conditions uniformly from  $(\varphi_{d,0}, \varphi_{q,0}, p_0) \sim [-0.5, 0.5]^2 \times [-1, 1]$ .

In this example,  $J$  is the state-dependent part of the pH model. As in Figure 8 and as in the previous examples, we noticed that the pH model outperforms the baseline when enough data is available for training. In addition, if we include the prior information that  $R$  and  $B$  are constant and the Hamiltonian is quadratic, we obtain significantly better results.

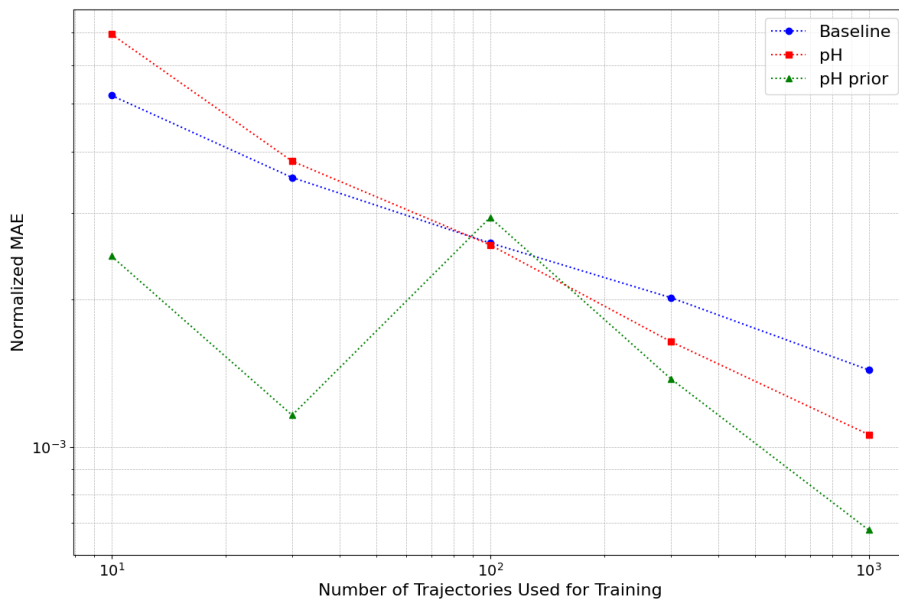
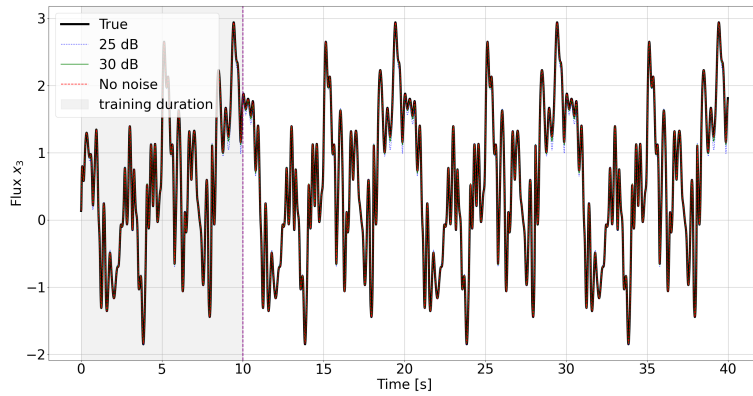


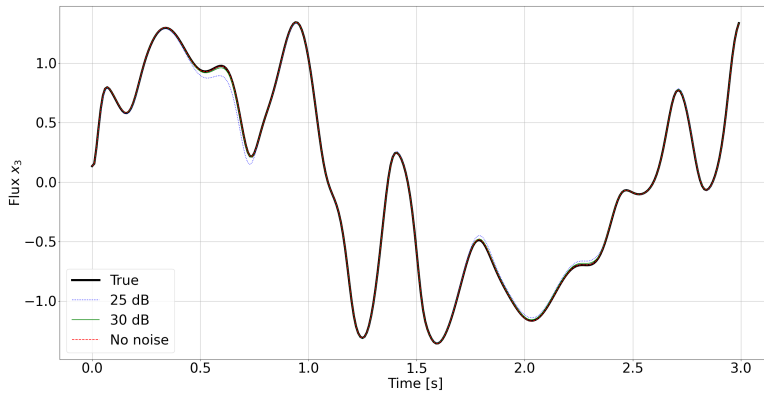
Figure 8: Average validation error for the motor example as a function of varying quantities of trajectories employed in training a baseline model, a default pH setup, and a pH setup incorporating prior knowledge.

Furthermore, for this example, we consider a preliminary study on noisy data. Uniform white noise was added to the inputs and outputs during training, while the states and derivatives of these were kept noise-free. Different levels of noise are compared in Figure 9 for the prediction of the flux. In this case, only

10 trajectories were used for training. The pH model based on the data without noise perfectly predicts the true trajectory, which shows that our method can also handle the state dependence in the  $J$  matrix of the pH model. In addition, as Figure 9 shows, our method can also handle noise in the data up to 30 dB without any deterioration in prediction quality. Starting from 25 dB, we start to notice a slight deviation in the state trajectory after zooming in on the first 3 seconds in Figure 9b. These preliminary results on the effect of noise in the data on the learned model are promising. A more comprehensive investigation into the impact of noise on our physics-based models is beyond the scope of this paper and will be addressed in future work.



(a) State trajectory and prediction up to 40 seconds.



(b) Zoom in on the first 3 seconds of the flux trajectory

Figure 9: Flux trajectory of the ball example based on the pH model with different noise levels in the training data.

#### 4.4 Discussion: MLP vs. KAN

Finally, we compare the MLP approach with the recent KAN approach. Here, we first studied the KAN baseline with the MLP baseline for all previous examples. For each example, we choose a number of trajectories that is enough to obtain reasonable results. As shown in Table 10, the NMAE of the KAN baseline is, for the ball and the spring example, one order of magnitude worse than the MLP baseline and for the motor the NMAE for the MLP baseline is 0.0076 whereas the KAN baseline has an NMAE of 0.143. Although KANs are better for the interpretability of the model since only a few neurons are used, due to this large error and the long training time required for KANs, we did not use KANs to approximate the parameters  $\theta_\bullet$  in the pH representation (4). However, there are more recent and efficient implementations of KAN [29, 50], which combine splines with radial basis functions that must be considered in future experiments.

	Ball	Spring	Motor
$N_{\text{tra}}$	100	10	10
KAN	0.044	0.037	0.143
MLP	0.0021	0.0065	0.0076

Figure 10: Comparison of NMAE for KAN and MLP.

As a summary, from our experiments, we noticed that incorporating physics using the port-Hamiltonian framework yields better results than baseline MLP and KAN for the system identification of nonlinear systems. If additional information about the model is available, such as the linearity of certain components, it can be integrated into the framework, leading to a significant reduction in validation error. In addition, we noticed that the pH models are better at longer time predictions, since they are able to capture the underlying physics of the system and not just replicate the training data as for the baseline.

## 5 Conclusion

We proposed a technique for the identification of system matrices for nonlinear port-Hamiltonian systems utilizing input-state-output data. The data is used to approximate each system matrix  $J$ ,  $R$  and  $B$  as well as the Hamiltonian  $H$  with a multilayer perceptron (MLP), a Kolmogorov-Arnold network (KAN), or, whenever prior information is available, a weighted combination of ansatz functions. The weights are subsequently optimized using the provided data. The effectiveness of our approach is demonstrated through several examples that exhibit nonlinearities in skew-symmetric components, dissipative terms, or the Hamiltonian. Future research will explore applications to more extensive examples, potentially derived from discretized partial differential equations, and will focus on identification from solely input-output data that may be incomplete.

## References

- [1] <https://github.com/Blealtan/efficient-kan>, 2024.
- [2] T. Beckers, J. Seidman, P. Perdikaris, and G. J. Pappas. Gaussian process port-Hamiltonian systems: Bayesian learning with physics prior. In *2022 IEEE 61st Conference on Decision and Control (CDC)*, pages 1447–1453, 2022.
- [3] P. Benner, P. Goyal, and P. Van Dooren. Identification of port-Hamiltonian systems from frequency response data. *Systems Control Lett.*, 143:104741, 2020.
- [4] S. L. Brunton, J. L. Proctor, and J. N. Kutz. Discovering governing equations from data by sparse identification of nonlinear dynamical systems. *Proceedings of the National Academy of Sciences*, 113(15):3932–3937, Mar. 2016.
- [5] F. L. Cardoso-Ribeiro, G. Haine, Y. Le Gorrec, D. Matignon, and H. Ramirez. Port-Hamiltonian formulations for the modeling, simulation and control of fluids. *Comput. & Fluids*, 283:106407, 2024.
- [6] R. Q. Chen, Y. Rubanova, J. Bettencourt, and D. K. Duvenaud. Neural ordinary differential equations. In *Advances in Neural Information Processing Systems 31 (NeurIPS 2018)*, 2018.
- [7] K. Cherifi. An overview on recent machine learning techniques for port Hamiltonian systems. *Phys. D*, 411:132620, 2020.
- [8] K. Cherifi and A. Brugnoli. Application of data-driven realizations to port-Hamiltonian flexible structures. *IFAC-PapersOnLine*, 54(19):180–185, 2021.
- [9] K. Cherifi, P. Goyal, and P. Benner. A non-intrusive method to inferring linear port-Hamiltonian realizations using time-domain data. *Electronic Transactions on Numerical Analysis : Special Issue SciML*, 56:102 – 116, 2022.
- [10] K. Cherifi, V. Mehrmann, and K. Hariche. Numerical methods to compute a minimal realization of a port-Hamiltonian system. *arXiv preprint arXiv:1903.07042*, 2019.
- [11] G. Cybenko. Approximation by superpositions of a sigmoidal function. *Math. Control Signals Systems*, 2:303–314, 1989.
- [12] A. Desai, L. Li, I. Chakrabarty, C. Bajaj, and S. Gupta. Port-Hamiltonian neural networks for constrained mechanical systems. In *arXiv preprint arXiv:2106.13188*, 2021.

- [13] H. Dänschel, L. Lentz, and U. von Wagner. Error measures and solution artifacts of the harmonic balance method on the example of the softening Duffing oscillator. *Journal of Theoretical and Applied Mechanics*, 62(2):435–455, 2024.
- [14] S. Eidnes, A. Stasik, C. Sterud, E. Bøhn, and S. Riemer-Sørensen. Pseudo-Hamiltonian neural networks with state-dependent external forces. *Phys. D*, 446:133673, 2023.
- [15] S. Elfving, E. Uchibe, and K. Doya. Sigmoid-weighted linear units for neural network function approximation in reinforcement learning. *Neural Networks*, 107:3–11, 2018.
- [16] M. Finzi, K. A. Wang, and A. G. Wilson. Simplifying Hamiltonian and Lagrangian neural networks via explicit constraints. In *Advances in Neural Information Processing Systems*, 2020.
- [17] H. Gernandt, F. Haller, T. Reis, and A. van der Schaft. Port-Hamiltonian formulation of nonlinear electrical circuits. *J. Geom. Phys.*, 159:103959, 2021.
- [18] H. Gernandt, B. Severino, X. Zhang, V. Mehrmann, and K. Strunz. Port-Hamiltonian modeling and control of electric vehicle charging stations. *IEEE Trans. Transportation Electrification*, 2024.
- [19] P. Goyal, P. Dollár, R. Girshick, P. Noordhuis, L. Wesolowski, A. Kyrola, A. Tulloch, Y. Jia, and K. He. Accurate, large minibatch SGD: Training ImageNet in 1 hour, 2018.
- [20] S. Greydanus, M. Dzamba, and J. Yosinski. Hamiltonian neural networks. In H. Wallach, H. Larochelle, A. Beygelzimer, F. d'Alché-Buc, E. Fox, and R. Garnett, editors, *Advances in Neural Information Processing Systems*, volume 32. Curran Associates, Inc., 2019.
- [21] V. L. Guen and N. Thome. Disentangling physical dynamics from unknown factors for unsupervised video prediction. In *2020 IEEE/CVF Conference on Computer Vision and Pattern Recognition (CVPR)*, pages 11471–11481, 2020.
- [22] M. Günther, B. Jacob, and C. Totzeck. Data-driven adjoint-based calibration of port-Hamiltonian systems in time domain. *Math. Control Signals Systems*, 36:957–977, 2024.
- [23] M. Günther, B. Jacob, and C. Totzeck. Structure-preserving identification of port-Hamiltonian systems—a sensitivity-based approach. In *Scientific Computing in Electrical Engineering, M. van Beurden et al., ed.*, pages 167–174, Cham, 2024. Springer Nature Switzerland.
- [24] T. Hastie, R. Tibshirani, and J. Friedman. *Neural Networks*, pages 389–416. Springer New York, New York, NY, 2009.

- [25] K. Hornik, M. Stinchcombe, and H. White. Multilayer feedforward networks are universal approximators. *Neural Networks*, 2(5):359–366, 1989.
- [26] B. Jacob and C. Totzeck. Port-Hamiltonian structure of interacting particle systems and its mean-field limit. *Multiscale Model. Simul.*, 22(4):1247–1266, 2024.
- [27] D. P. Kingma. Adam: A method for stochastic optimization. *arXiv preprint arXiv:1412.6980*, 2014.
- [28] J. Lei Ba, J. R. Kiros, and G. E. Hinton. Layer normalization. *arXiv preprint arXiv:1607.06450*, 2016.
- [29] Z. Li. Kolmogorov-Arnold Networks are radial basis function networks, 2024.
- [30] Z. Liu and Y. Wang. KAN: Kolmogorov–Arnold networks. *arXiv preprint arXiv:2406.07819*, 2024.
- [31] M. Lohmayer and S. Leyendecker. EPHS: A port-Hamiltonian modelling language. *IFAC-PapersOnLine*, 55(30):347–352, 2022.
- [32] N. Lopes, T. Hélie, and A. Falaize. Explicit second-order accurate method for the passive guaranteed simulation of port-Hamiltonian systems. *IFAC-PapersOnLine*, 48(13):223–228, 2015.
- [33] I. Loshchilov. Decoupled weight decay regularization. *arXiv preprint arXiv:1711.05101*, 2017.
- [34] I. Loshchilov and F. Hutter. SGDR: Stochastic gradient descent with warm restarts, 2017.
- [35] S. O. Medianu. *Identification of Port Hamiltonian systems*. Theses, Université Grenoble - Alpes, 2017.
- [36] V. Mehrmann and B. Unger. Control of port-Hamiltonian differential-algebraic systems and applications. *Acta Numerica*, pages 395–515, 2023.
- [37] R. Morandin, J. Nicodemus, and B. Unger. Port-Hamiltonian dynamic mode decomposition. *SIAM J.Sci. Comput.*, 45(4):A1690–A1710, 2023.
- [38] J. Najnudel, R. Müller, T. Hélie, and D. Roze. Identification of nonlinear circuits as port-Hamiltonian systems. In *2021 24th International Conference on Digital Audio Effects (DAFx)*, pages 1–8, 2021.
- [39] C. Neary and U. Topcu. Compositional learning of dynamical system models using port- Hamiltonian neural networks. In *Proceedings of Machine Learning Research vol 211:1–17, 2023 5th Annual Conference on Learning for Dynamics and Control*, 2023.

- [40] A. Paszke, S. Gross, F. Massa, A. Lerer, J. Bradbury, G. Chanan, T. Killeen, Z. Lin, N. Gimelshein, L. Antiga, A. Desmaison, A. Köpf, E. Yang, Z. DeVito, M. Raison, A. Tejani, S. Chilamkurthy, B. Steiner, L. Fang, J. Bai, and S. Chintala. Pytorch: An imperative style, high-performance deep learning library, 2019.
- [41] T. Pfaff, M. Fortunato, A. Sanchez-Gonzalez, and P. Battaglia. Learning mesh-based simulation with graph networks. In *International Conference on Learning Representations*, 2021.
- [42] C. Ponce, Y. Wu, Y. Le Gorrec, and H. Ramirez. A systematic methodology for port-Hamiltonian modeling of multidimensional flexible linear mechanical systems. *Appl. Math. Model.*, 134:434–451, 2024.
- [43] M. Raissi, P. Perdikaris, and G. E. Karniadakis. Physics-informed neural networks: A deep learning framework for solving forward and inverse problems involving nonlinear partial differential equations. *J. Comput. Phys.*, 378:686–707, 2019.
- [44] J. Rettberg, J. Kneifl, J. Herb, P. Buchfink, J. Fehr, and B. Haasdonk. Data-driven identification of latent port-Hamiltonian systems. In *arXiv preprint arXiv:2408.03212*, 2024.
- [45] P. Schwerdtner. Port-Hamiltonian system identification from noisy frequency response data, 2021.
- [46] P. Schwerdtner, T. Moser, V. Mehrmann, and M. Voigt. Structure-preserving model order reduction for index one port-Hamiltonian descriptor systems. *ArXiv*, 2022.
- [47] P. Schwerdtner, P. Schulze, J. Berman, and B. Peherstorfer. Nonlinear embeddings for conserving Hamiltonians and other quantities with Neural Galerkin schemes. *SIAM J. Sci. Comput.*, 46(5):C583–C607, 2024.
- [48] P. Schwerdtner and M. Voigt. SOBMOR: Structured optimization-based model order reduction. *SIAM J. Sci. Comput.*, 45(2):A502–A529, 2023.
- [49] M. Spirito, Y. Le Gorrec, and B. Maschke. Structure-preserving observers for port-Hamiltonian systems via contraction analysis. *IEEE Trans. Automat. Control*, July 2023.
- [50] H.-T. Ta. BSRBF-KAN: A combination of B-splines and radial basis functions in Kolmogorov-Arnold Networks, 2024.
- [51] P. Toth, D. J. Rezende, A. Jaegle, S. Racanière, A. Botev, and I. Higgins. Hamiltonian generative networks. In *International Conference on Learning Representations*, 2020.
- [52] A. J. van der Schaft and D. Jeltsema. Port-Hamiltonian Systems Theory: An Introductory Overview. *Foundations and Trends® in Systems and Control*, 1(2-3):173–378, 2014.

- [53] G. J. E. van Otterdijk, S. Moradi, S. Weiland, R. Tóth, N. O. Jaensson, and M. Schoukens. Learning subsystem dynamics in nonlinear systems via port-Hamiltonian neural networks, 2024.
- [54] A. Vaswani, N. Shazeer, N. Parmar, J. Uszkoreit, L. Jones, A. N. Gomez, L. Kaiser, and I. Polosukhin. Attention is all you need, 2023.
- [55] P. Virtanen, R. Gommers, T. E. Oliphant, M. Haberland, T. Reddy, D. Cournapeau, E. Burovski, P. Peterson, W. Weckesser, J. Bright, et al. Scipy 1.0: fundamental algorithms for scientific computing in python. *Nature methods*, 17(3):261–272, 2020.
- [56] N. M. T. Vu, T. H. Pham, I. Prodan, and L. Lefèvre. Port-Hamiltonian observer for state-feedback control design. In *European Control Conference, ECC 2023, Bucharest, Romania, June 13-16, 2023*, pages 1–6. IEEE, 2023.
- [57] Y. Yin, V. L. Guen, J. Dona, E. de Bézenac, I. Ayed, N. Thome, and P. Gallinari. Augmenting physical models with deep networks for complex dynamics forecasting. *J. Stat. Mech. Theory Exp.*, 2021(12):124012, 2021.
- [58] P. Zaspel and M. Günther. Data-driven identification of port-Hamiltonian DAE systems by Gaussian processes. *arXiv preprint arXiv:2406.18726*, 2024.